Reliable and Efficient Reaction Path and Transition State Finding for Surface Reactions with the Growing String Method

Mina Jafari and Paul M. Zimmerman*

The computational challenge of fast and reliable transition state and reaction path optimization requires new methodological strategies to maintain low cost, high accuracy, and systematic searching capabilities. The growing string method using internal coordinates has proven to be highly effective for the study of molecular, gas phase reactions, but difficulties in choosing a suitable coordinate system for periodic systems has prevented its use for surface chemistry. New developments are therefore needed, and presented herein, to handle surface reactions which include atoms with large coordination numbers that cannot be treated using standard internal coordinates. The double-ended and single-ended growing string methods are implemented using a hybrid coordinate system, then benchmarked for a test set of 43 elementary reactions occurring on surfaces. These results show that the growing string method is at least 45% faster than the widely used climbing image-nudged elastic band method, which also fails to converge in several of the test cases. Additionally, the surface growing string method has a unique single-ended search method which can move outward from an initial structure to find the intermediates, transition states, and reaction paths simultaneously. This powerful explorative feature of single ended-growing string method is demonstrated to uncover, for the first time, the mechanism for atomic layer deposition of TiN on Cu(111) surface. This reaction is found to proceed through multiple hydrogen-transfer and ligand-exchange events, while formation of H-bonds stabilizes intermediates of the reaction. Purging gaseous products out of the reaction environment is the driving force for these reactions. © 2017 Wiley Periodicals, Inc.

Introduction

The information contained in transition state (TS) structures and reaction paths (RP) provides the fundamental atomistic details of reaction mechanisms. From a computational viewpoint, TSs are first-order saddle points on a potential energy surface (PES) representing the connection of two intermediates along a path. The high dimensionality of most PESs, however, makes TS-finding an impossible task unless fast, reliable, and accurate methods are available. Given the great interest in simulation of reactions on surfaces, such as atomic layer deposition (ALD),[1] heterogeneous catalysis,[2,3] and electrochemical CO_2 reduction,[4] novel tools for TS and RP finding are in demand.

The algorithms designed to locate TSs and RPs are usually classified as single-ended[5–54] or double-ended.[55–98] Single-ended methods start from a single initial state and refine it systematically to locate a TS. Many single-ended methods require an initial guess geometry lying close to the desired TS structure, which limits the effectiveness of these approaches. Double-ended methods, conversely, connect two structures in a discretized RP and are usually more reliable than single-ended methods due to the endpoints of the path being fixed, so double-ended methods are less likely to diverge to undesired search regions. Most double-ended algorithms do not compute the exact saddle point, so they are usually followed by a local search method (such as the dimer method,[15] mode-tracking,[52] or eigenvector following method[14,34]) to refine the apparent TS structure to the exact TS.[99]

Given the multitude of methods available for TS and RP finding, these techniques are best summarized by the key components that afford their success. We classify these in four groups: (1) Strategies for quickly approaching the vicinity of the saddle point, (2) Estimation of the direction of negative curvature, (3) Optimizer, and (4) Coordinate system, which should all operate synergistically to rapidly and reliably locate TSs. In an ideal search algorithm, the combination of these four components should operate with little input from the user. These four areas will now be discussed to set the context for our proposed method.

Starting from an initial state, there are three often-used algorithmic strategies to approach the saddle point region. Minimum-mode following methods find the lowest curvature direction of the Hessian and follow this eigenvector toward the saddle point.[48,100] Alternatively, coordinate driving techniques push the initial structure toward an approximate TS structure along a specified reaction direction.[23,31,101] When the initial and final states are known, the highest energy point along an approximate RP from a double-ended method can be used as a good estimate of the exact TS.[60,99]

M. Jafari, P. M. Zimmerman
Department of Chemistry, University of Michigan, 930 N. University Ave,
Ann Arbor, Michigan 48109 E-mail: paulzim@umich.edu

After obtaining an approximate TS geometry, the direction corresponding to the transition vector must be estimated. While in principle the exact Hessian can be calculated and diagonalized to find the negative curvature direction, the computational cost can be expensive or prohibitive. To reduce this cost, approximate Hessians can be constructed and diagonalized via subspace iteration methods,[48,102–104] or alternatively, the reaction tangent at the guess TS from a RP can provide an estimate of this direction.[99]

In addition to the two prerequisites of a good initial TS structure and reaction direction, an efficient optimizer[34] is necessary to direct the TS searches and refine the RP. In practice, quasi-Newton[34] methods are widely used because they update approximate Hessians at each optimization step, entirely skipping Hessian computations while still benefiting from PES curvature information. For TS searches, eigenvector following optimizers[99] maximize the energy along the lowest Hessian mode while minimizing in all other directions. These methods tend to converge when the Hessian contains a reasonably accurate eigenvector representing the reaction direction.

The fourth component of interest is the coordinate system which forms the basis in which RPs and TSs are optimized. Cartesian coordinates are often chosen due to their simple implementation, despite internal coordinates (IC) being superior in many respects: chemical bonds are included as intrinsic coordinates, the curvilinear motion of angle bending or torsions are better represented by internals, and ICs have reduced intercoordinate coupling which allows faster optimization. Further advantages include that the interpolation of a RP in ICs avoids the collision of atoms or intersections of bonds,[9,11,12,23,34,54,57,86,99] and ICs can accelerate convergence of optimization by a factor of four.[18,57,58,105]

Two common surface-compatible reaction finding methods are the nudged elastic band[62] (NEB) and the dimer[15] method. NEB and its variations[59,60,63,64] interpolate between two structures in Cartesian coordinates to optimize a chain-of-states representation of the RP. NEB, therefore, is frequently used to form the guess for a TS optimization by the dimer method in a two-step procedure. Multi-step computational procedures are inherently less user-friendly, suggesting new methods for simultaneous RP and TS finding with increased efficiency, reliability, and usability as promising additions to the computational toolkit.

Herein a novel means for systematic TS search and RP finding is implemented in a powerful tool for the study of surface reactions. The method is inspired by GSM[54,65,86,99] and designed as a combined RP optimization and TS search algorithm. When the reactant and product structures are known, the new double-ended GSM (DE-GSM) can be used to calculate a RP and TS at low cost and high fidelity. In cases where the final structure is unknown, single-ended GSM (SE-GSM) can explore a new reaction space based on simple reaction coordinates as input. Detailed comparisons of three investigated methods (DE-, SE-GSM, and CI-NEB) are provided to benchmark their computational cost and reliability. The high usability of SE-GSM for exploring new reactions is

demonstrated by showing an atomistic mechanism for the initiation and growth of titanium nitride on Cu(111) surface.

Method

Growing string method with exact TS search

Overview. GSM develops a RP by iteratively adding new nodes and optimizing them until a complete RP with a TS and a stable intermediate on each side of the string are present. The string consists of a discretized set of structures along the RP connecting the reactant and product geometries and is constructed starting only from the endpoints. By incremental addition of new nodes, GSM rapidly leads to a reasonably well converged RP as it avoids placing nodes at high-energy regions of the PES.[65]

Based on our experience using GSM for molecular systems,[54,86,99] we have developed a new method to overcome challenges of RP and TS finding for periodic systems and surface reactions. This method operates through three overall phases: growth, optimization, and exact TS search (Supporting Information Figure S1), which now will be discussed in detail.

Growth Phase. During the growth phase, new nodes are added along the reaction tangent direction and minimized in directions perpendicular to the reaction tangent. The reaction tangent is defined either by interpolation or driving coordinates (see below), and used as a constraint to prevent nodes from falling back to local minima. New nodes are added after the gradient at the frontier node drops below a predefined threshold, and the growth phase terminates when either two string fragments are connected (double-ended) or an intermediate on the other side of the string is found (single-ended).

The tangent definition during the growth phase depends on whether the algorithm is double-ended or single-ended. For DE-GSM, the reaction tangent for node i pointing to node j is defined as

$$U_C = \alpha_c \sum_k \langle \Delta q | U_k^{(i)} \rangle U_k^{(i)} \tag{1}$$

where U_C is the (constrained) tangent direction, Δq is defined to be $\Delta q = q^{p,(j)} - q^{p,(i)}$, q^P are the primitive (hybrid) coordinates, α_c is a normalization factor, and the vectors U_k are the nonredundant (NR) (hybrid) coordinates vectors (see Coordinate System for Surfaces). Following the constrained optimization in delocalized IC introduced by Baker et al.,[12] Δq is projected onto the NR DOF and then normalized to form a vector space with one extra DOF. The new vector set undergoes Schmidt orthonormalization to form a new coordinate set spanning the constraint vector U_C and the remaining NR DOF. This procedure allows a RP to be represented in any combination of internal and Cartesian coordinates without any problems caused by an over-specified (redundant) set of coordinates.

SE-GSM requires a modification in the tangent definition for the growth phase

$$U_C = \alpha_c \sum_{k=1}^{3N-6} \langle \delta q | U_k^{(i)} \rangle U_k^{(i)} \qquad (2)$$

where δq is a primitive coordinate vector describing desired changes in connectivity (bond lengths, angles, and torsions). During the growth phase, new nodes are added, one at a time, along the vector U_C and only this frontier node is optimized using U_C as a constraint.

Combining GSM with IC, therefore, allows an opportunity of using driving coordinates to find TSs starting from a single initial state. The resulting method, SE-GSM, can explore the chemical reaction space without having prior knowledge about the final state. In practice, δq includes reaction coordinates (combination of bonds, angles, and torsions) representing any desired reaction. This includes coordinates not present in the primitive internals of the starting structure, as any reaction coordinates can be trivially added to the coordinate system when needed.

Optimization. When the string is fully grown, all the nodes on the string undergo optimization cycles under the constraint U_C of eq. (1), which depends on the node's location along the string. During optimization, an approximate Hessian matrix is used to accelerate convergence. This Hessian is formed when a node is created from a diagonal primitive coordinate Hessian,[99] and updated using the BFGS[106–109] scheme as optimization proceeds. Diagonalization of the Hessian at each node in the NR coordinates provides a set of eigenvectors and eigenvalues which are used in the eigenvector optimizer:

$$\Delta v_i = \frac{-g_i}{H_{ii} + \lambda} \qquad (3)$$

v_i are the eigenvectors of the Hessian in coordinates U_k, H_{ii} are the corresponding eigenvalues, g_i is the gradient in the eigenvector basis, and λ is a scaling factor.

After the RP is converged to a specified threshold, a CI search begins.[60] At the TS node, perpendicular directions are optimized as described by eq. (3) while the U_C direction of the highest energy node is maximized according to:

$$\Delta U_C = \frac{g_c}{\beta} \qquad (4)$$

U_C is the constraint climbing direction, g_c is the gradient along the U_c, and β is a scaling constant.

The CI search [eq. (4)] moves the highest energy node toward the vicinity of the saddle point, which is vital to providing an accurate TS guess prior to the exact TS search. At this point, the reaction tangent (U_C) also provides a good approximation to the TS eigenmode.

Exact TS search. After the CI search has begun and the RP converges to a predefined gradient threshold, the eigenvector following TS search commences. The eigenvector of the Hessian with highest overlap with the reaction tangent ($\max_i \langle U_C | v_i \rangle$) at the TS node is followed to find the exact TS

$$\Delta v_{RP} = \frac{g_{RP}}{H_{RP} + \lambda} \qquad (5)$$

where subscript RP refers to the vector with maximum overlap. This strategy ensures the correct mode is followed,[99] but requires that the RP be available during the TS search. Therefore, GSM with exact TS search has a particular advantage over typical saddle point finding methods which do not simultaneously optimize the RP.

Prior to beginning the TS optimization, the Hessian has no negative eigenvalues because the BFGS scheme enforces a positive definite Hessian. To initiate the exact TS search, the curvature along RP is approximated using the RP tangent defined by the nodes neighboring the TS. Projecting this curvature into the Hessian results in a single negative eigenvalue and its corresponding eigenvector, while avoiding the (expensive) computation of the exact Hessian. Details on building this Hessian can be found in the Appendix.

Coordinate system for surfaces

As many studies have shown,[9,11–13,18,27,32,34,57,86,110] the motion of molecular systems is best described by IC, which are composed of primitive coordinates such as bonds, angles, and torsions. A specifically useful type of ICs are delocalized ICs[12] which are constructed from a set of primitive internals[9] and fully span the NR coordinate space. These coordinates can be used whenever a set of primitives is available, and provide the significant benefit for optimization of systems including atoms with low coordination numbers.

Use of any type of IC becomes significantly more cumbersome, however, when treating periodic systems which include a large number of atoms with high coordination numbers. For instance with metallic systems, optimizing using ICs is impractical due to the huge number of primitive coordinates that can be present. A mixed coordination system involving Cartesians on high coordination number atoms, and ICs elsewhere, is straightforward.[110,113,114]

Such a mixed coordinate system is justified because in a surface reaction only certain atoms require ICs, while others are largely immobile. For instance in a typical reaction, adsorbate atoms move significantly while surface atoms remain relatively immobile and act as binding sites for adsorbate species. Furthermore, only the surface's topmost layer is actively involved in a reaction and bottom layers are stationary supports. As a result, there is no obvious need to include all atoms in the IC set, as Cartesians will easily be able to describe relatively immobile atoms.

Fortunately, a hybrid coordinate system is fully compatible with the delocalized IC procedure. For each reaction, we define the active surface atoms involved, and assign ICs to these atoms along with all molecular species in the system. All atoms embedded in the surface are assigned Cartesian coordinates, as shown in Figure 1. Once the (redundant) set of Cartesians and ICs are available, the delocalized hybrid coordinates are formed with the usual procedure (see Appendix).
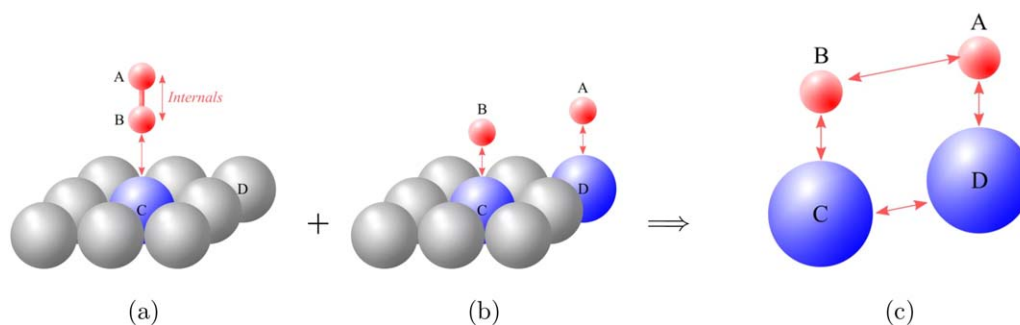
Figure 1. Illustration of the hybrid coordinate system for bonds. a), b), and c) show bonds in reactant, product, and the union, respectively. Red and blue atoms indicate adsorbate and active surface species, respectively (red: IC only, blue: IC and Cartesians, gray: Cartesians only). Double arrows denote a bond between two atoms. [Color figure can be viewed at wileyonlinelibrary.com]

Computational details

All energy and gradient calculations are performed in a plane wave basis set under periodic boundary conditions as implemented in the Vienna *Ab Initio* Simulation Package (VASP).[115–118] The PBE functional and projector-augmented wave methods are used to describe the exchange-correlation energy and electron-ion interactions, respectively. An energy cutoff of 300 eV and a smearing parameter of 0.2 eV were used for the plane waves. The Brillouin zone is sampled using a $1 \times 1 \times 1$ Monkhorst-Pack mesh for all reactions except reactions 5, 7, and 9 where a $2 \times 2 \times 1$ k-point grid is used for the integration and the energy cutoff is set to 400 eV. GSM is implemented in C++ and invokes the Atomistic Simulation Environment (ASE)[119] to provide the quantum mechanical gradients through VASP.

For both single-ended and DE-GSM, the equal spacing of the nodes on each side of the TS node is maintained by a reparameterization step that is performed after each optimization cycle. Reparameterization does not shift the highest energy node after string is fully grown and CI starts.

All CI-NEB calculations used the BFGS optimizer as implemented in ASE and a spring constant of 0.1 eV/Å. CI-NEB were considered converged when the RMS gradient on the TS node was below 0.0136 eV/Å $\simeq$ 0.0005 Hartree/Å and the total gradient over all the active images was below 2.7 eV/Å $\simeq$ 0.1 Hartree/Å to match the GSM's convergence criteria. The calculations that required more than 200 gradient computations per active node (>1,800 gradient calculations for double-ended methods) were terminated and considered unsuccessful.

The chemical structures for this study are created using ASE and the CI-NEB method is used as implemented in ASE. Reactant and product structures were optimized using the BFGS Line Search optimizer and were converged when the maximum force on each atom was below 0.05 eV/Å.

In the examples that follow, 11 nodes including the two fixed endpoints (9 active nodes) were used to represent the RP for double-ended calculations (DE-GSM and CI-NEB) except reaction 1, which has 7 nodes. The input reactant and product structures for the double-ended methods are identical for both methods. The number of nodes for SE-GSM is determined by the method automatically, and typically ranges from 7 to 11 nodes in the reported tests. The three methods under study are compared based on the number of gradient computations required for the convergence of the RP and calculated activation barriers. More details can be found in section 1 of Supporting Information.

Surface reaction validation test set

To confirm the efficiency and reliability of the proposed method, an extensive test set of elementary reactions was created. A variety of reaction types, including molecular and dissociative adsorptions, desorptions, and bimolecular and unimolecular reactions, are covered in this set. Most of these reactions have been investigated previously using the NEB method by other researchers.[120–135] In summary, 43 elementary reactions which consists of nine different metals, one metal oxide, and seven different surface terminations were studied. Summaries of the reactions are given in Table 1.

Results and Discussion

Overall performance of reaction path optimization methods

To evaluate the performance and stability of the three reaction finding methods, their computational cost and success rate will be compared first. Robust methods should converge relatively fast on a wide variety of reactions and successfully calculate a RP and TS in a small number of gradient calculations. The success rate and average number of gradient calls for convergence of DE-GSM, SE-GSM, and CI-NEB are shown in Figure 2. DE-GSM was successful in all cases (43 out of 43) while SE-GSM succeeded for 41. CI-NEB converged in 33 out of 43 test cases within 1,800 total gradient calculations, and the reasons for the failures will be discussed in the subsequent section. The average number of gradient calls were 614, 338, and 366 for CI-NEB, DE-GSM, and SE-GSM, respectively, demonstrating that GSM is on average at least 1.8 times faster than CI-NEB.

Taking a closer look at the convergence behavior of the methods provides some insight into the faster convergence of GSM. An example is shown in Figure 3 where an addition reaction on Pd(111) (Reaction 8-b) takes place between a hydrogen atom and an ethyl fragment to form ethane. The initially interpolated RP from CI-NEB has a higher RMS gradient compared to DE-GSM's and, therefore, requires a larger number of

Table 1. Elementary step test cases for GSM.

ID	Reaction	ID	Reaction
1	$Au(fcc) \xrightarrow{Pt(111)} Au(hcp)$	11-a	$OH^* + H^* \xrightarrow{Cu(100)} H_2O^*$
2	$CO(fcc) \xrightarrow{Pd(111)} CO(hcp)$	11-b	$CO^* + O^* \xrightarrow{Cu(100)} CO_2^*$
3-a	$CO + O \xrightarrow{Pd(111)} CO_2^*$	12-a	$OH^* + H^* \xrightarrow{Cu(111)} H_2O^*$
3-b	$CO_2^* \xrightarrow{Pd(111)} CO_2 (g)$	12-b	$CO^* + O^* \xrightarrow{Cu(111)} CO_2^*$
4-a	$CO + O \xrightarrow{Ru(0001)} CO_2^*$	13-a	$OH^* + H^* \xrightarrow{Cu(110)} H_2O^*$
4-b	$CO_2^* \xrightarrow{Ru(0001)} CO_2 (g)$	13-b	$CO^* + O^* \xrightarrow{Cu(110)} CO_2^*$
5-a	$H(fcc) \xrightarrow{Ni(111)} H(fcc)$	14-a	$H_2S^* \xrightarrow{W(111)} HS^* + H^*$
5-b	$H(fcc) \xrightarrow{Ni(111)} H(hcp)$	14-b	$HS^* \xrightarrow{W(111)} S^* + H^*$
5-c	$H(hcp) \xrightarrow{Ni(111)} H(fcc)$	14-c	$H^* + H^* \xrightarrow{W(111)} H_2 (g)$
6-a	$Cu(bridge) \xrightarrow{Cu(110)} Cu(hollow)$	15-a	$H_2O^* \xrightarrow{W(111)} HO^* + H^*$
6-b	$Cu(hollow) \xrightarrow{Cu(110)} Cu(hollow)$	15-b	$HO^* \xrightarrow{W(111)} O^* + H^*$
6-c	$Cu \xrightarrow{Cu(110)} Cu$ (atom swap)	16-a	$CH_2 = CHCH_2OH^* + O^* \xrightarrow{Au(111)}$ $CH_2=CHCH_2O^* + OH^*$
7-a	$CH_3CH_2COOH^* \xrightarrow{Pd(111)}$ $CH_3CH_2CO^* + OH^*$	16-b	$CH_2=CHCH_2O^* + O^* \xrightarrow{Au(111)}$ $CH_2=CHCH=O^* + OH^*$
7-b	$CH_3CH_2CO^* \xrightarrow{Pd(111)} CH_3CH_2^* + CO^*$	17-a	$CH_3OH^* \xrightarrow{Cu(110)} CH_3O^* + H^*$
8-a	$CH_2CH_2^* + H^* \xrightarrow{Pd(111)} CH_3CH_2^*$	17-b	$CH_3O^* \xrightarrow{Cu(110)} H_3C=O^* + H^*$
8-b	$CH_3CH_2^* + H^* \xrightarrow{Pd(111)} CH_3CH_3^*$	18-a	$CN^* + H^* \xrightarrow{Pt(111)} CNH^*$
9-a	$NH_3^* \xrightarrow{RuO_2(110)} NH_2^* + H^*$	18-b	$CNH^* + H^* \xrightarrow{Pt(111)} CNH_2^*$
9-b	$NH_2^* \xrightarrow{RuO_2(110)} NH^* + H^*$	19-a	$NH_3 (g) \xrightarrow{Si(111)-Cl} NH_3^*$
9-c	$2N^* \xrightarrow{RuO_2(110)} N_2^*$	19-b	$NH_3^* \xrightarrow{Si(111)-Cl} NH_2^* + HCl (g)$
9-d	$N^* + O^* \xrightarrow{RuO_2(110)} NO^*$	20	$H_2O (g) \xrightarrow{Si(111)-H} OH^* + H_2 (g)$
10-a	$CO^* + H^* \xrightarrow{Ni(111)} COH^*$	21	$CH_4 (g) \xrightarrow{Ir(111)} CH_3^* + H^*$
10-b	$COH^* + H^* \xrightarrow{Ni(111)} C^* + H_2O (g)$		

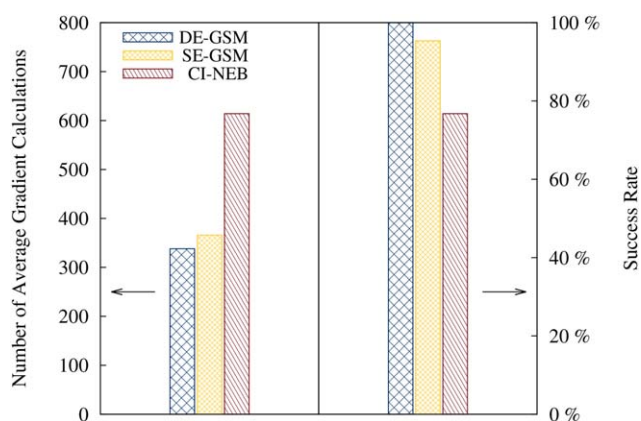Asterisks designate the surface species.

Figure 2. Average number of gradient calculations and success rate for each method. (Calculations with more than 1,800 gradient calculations are not included in the average gradient calculation). [Color figure can be viewed at wileyonlinelibrary.com]
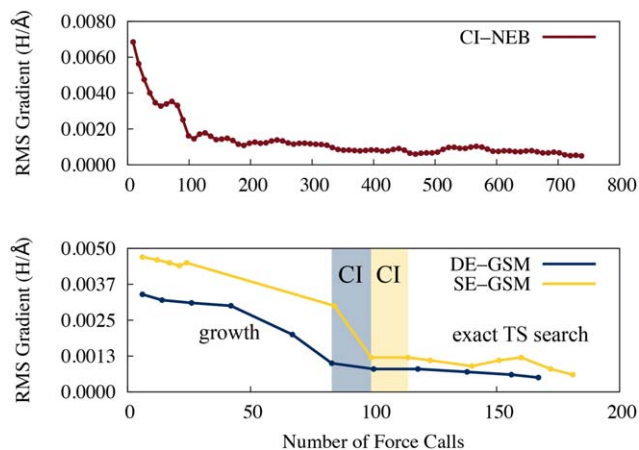

Figure 3. Convergence behavior of the methods plotted for reaction 8-b. CI-NEB has a higher initial RMS gradient compared to GSM in addition to larger RMSD of initial and final RPs, and therefore, more force calls are required to reach convergence. The gradient calls required for each phase of GSM calculations are labeled in the bottom plot. [Color figure can be viewed at wileyonlinelibrary.com]
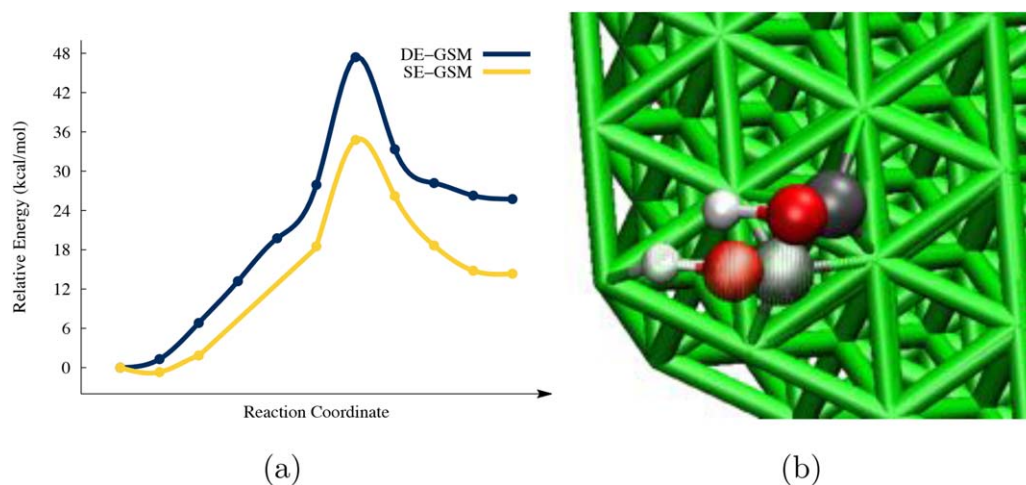
Figure 4. a) Reaction path calculated by DE-GSM (blue) and SE-GSM (yellow) for COH formation on Ni(111). b) TS structures calculated by DE-GSM (opaque) and SE-GSM (translucent). CO molecule is not stationary in the case of SE-GSM. [Color figure can be viewed at wileyonlinelibrary.com]

optimization iterations to converge. GSM, conversely, does not generate all of the nodes at once, which avoids distorted chemical structures with high gradients. This property of maintaining low gradients and small numbers of optimization steps is well-known for GSM,[65] and is fully taken advantage of in DE- and SE-GSM for surfaces.

Additionally, the initial linear path by CI-NEB does not capture the correct asynchronicity in hydrogen and carbon movements. On average, the carbon atom moves 0.03 Å higher on the surface in CI-NEB's initial path compared to DE-GSM. At the same time, the hydrogen is 0.04 Å closer to the surface in CI-NEB. The root mean square deviations (RMSD) in RPs indicate that DE-GSM's initial RP is similar to its final path (RMSD = 0.097), while CI-NEB's deviates more significantly (RMSD = 0.209). In CI-NEB, this difference is seen in the unnecessary half-circular motion of hydrogen adatom on surface before its addition to the ethyl group (Supporting Information Figures S16, S15 and Table S1). Overall, the high quality of GSM's initial RP results in improved performance compared to CI-NEB.

Comparison of reaction paths from DE-GSM and CI-NEB

To further demonstrate the reliability and robustness of DE-GSM, it will now be compared in more detail to the CI-NEB method. As shown in Supporting Information Figure S3, the activation energies predicted by these two methods are

similar, with a linear regression of slope 0.995 and R^2 of 0.989. This correlation shows that DE-GSM with its exact TS search produces similar barriers compared to those from CI-NEB. Some deviation is expected, however, because GSM performs an exact saddle point search, while CI-NEB provides an approximate TS. The maximum difference in calculated activation energies by two double-ended methods occurs for water dissociation on W(111) (Reaction 15-a), which differs by 4.6 kcal/mol between DE-GSM and CI-NEB. In section 2 of Supporting Information, we show that this difference occurs because the two methods find distinct reaction pathways, which should not have the same barrier.

There are two cases where CI-NEB did not compute a realistic RP, specifically two copper surface rearrangements,[136] reactions 6-b and 6-c. Such reaction steps are known to be important for copper-promoted graphene growth[137] and silicon device production,[138] and otherwise represent standard reactions that should be resolvable by double-ended methods. In Reaction 6-c, two Cu atoms exchange positions on Cu(110) surface, but the linear Cartesian interpolation of the CI-NEB's initial RP causes the moving atoms to sit directly on top of one another (section 2 of Supporting Information). From this geometry, convergence of the DFT density and energy fails, and optimization cannot proceed. DE-GSM, by incrementally adding and optimizing nodes, never reaches such problematic structures and optimizes smoothly to the desired RP. Reaction

Table 2. Bond lengths and angles for the reactant, TSs, and products of Reaction 10-a calculated by DE-GSM and SE-GSM. [Color table can be viewed at wileyonlinelibrary.com]

Bonds (Å) and angle	Reactant	DE-GSM		SE-GSM	
		Transition state	Product	Transition state	Product
C5-Ni1	2.037	1.965	1.892	1.940	1.884
C5-Ni2	2.082	1.939	1.949	3.287	3.187
C5-Ni3	1.856	1.800	1.803	1.870	1.849
C5-Ni4	3.114	2.974	2.991	1.880	1.863
C5-O6	1.189	1.273	1.339	1.280	1.348
O6-H7	3.557	1.349	0.981	1.311	0.983
∠ C5-O6-H7	60.3	88.2	111.0	96.7	107.3

Colored values indicate bonds and angles that are different in structures calculated by the methods. Both methods result in the same product while the product's position on the surface is different.
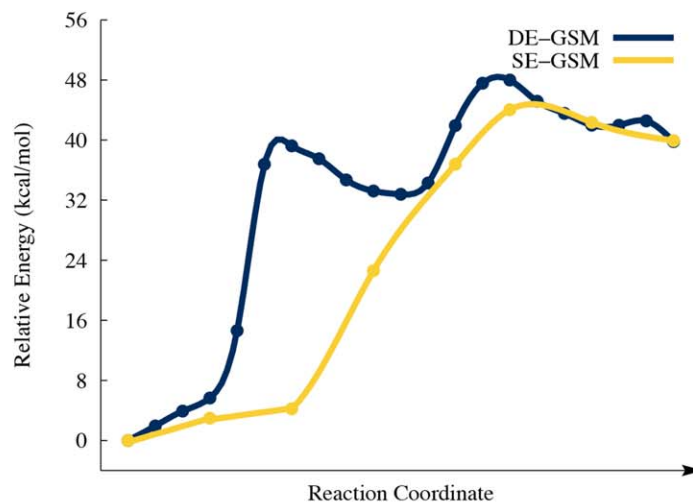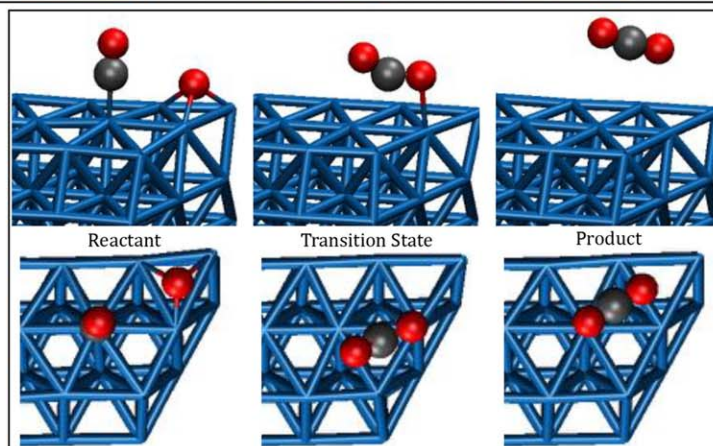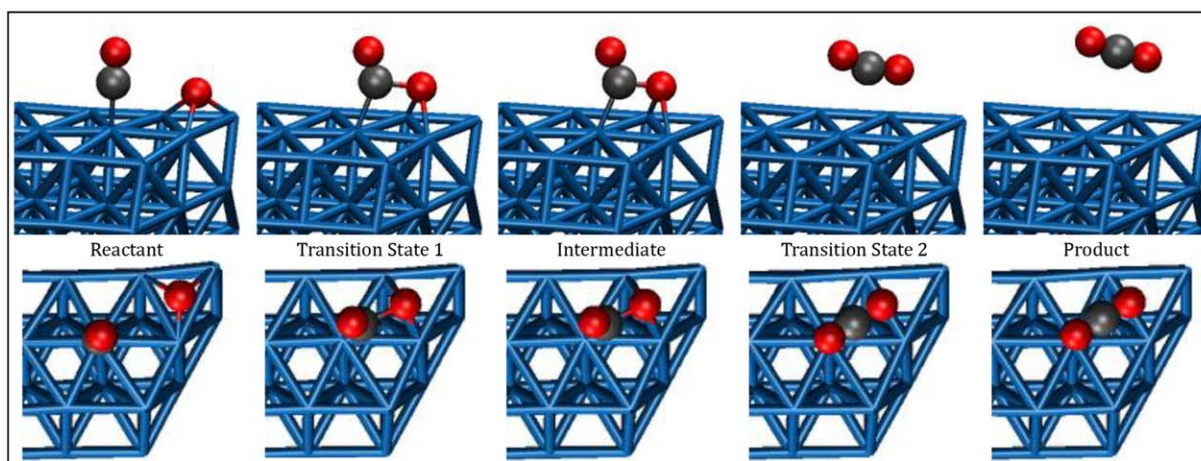
Figure 5. a) Reaction path calculated by DE-GSM (blue) and SE-GSM (yellow) for CO_2 formation on Ru(0001). b) Reactant, TS, and product structures for reaction (4) calculated by DE-GSM (top) and SE-GSM (bottom). Reaction proceeds in one and two elementary steps via SE-GSM and DE-GSM, respectively. [Color figure can be viewed at wileyonlinelibrary.com]

6-b similarly has a problem with the initial interpolation in CI-NEB, which is discussed in section 2 of Supporting Information.

Comparison of DE-GSM and SE-GSM

In the case of SE- and DE-GSM, the reaction tangent definitions are different and can lead to unique RPs being found for the same qualitative reaction. This can occur in reactive systems with more than a few degrees of freedom, where there are often multiple pathways from a given initial state to a single product structure.[34] Usually, TS finding methods locate only one such path at a time, and thus offer no guarantee that all connecting TSs will be found. Cases where two different RPs were found by SE- and DE-GSM are discussed in this section.

The activation energies computed by SE-GSM and DE-GSM (Supporting Information Figure S8) are usually similar, but less closely related than DE-GSM compared to CI-NEB. The comparison of SE- to DE-GSM yields a slope of 0.899 and R^2 value of 0.875. Because the optimization process is identical for the two methods after the string endpoints are connected, this slight dissimilarity is due to differences in the initial reaction tangent and RP. Specifically, as DE-GSM uses curvilinear interpolation in ICs between the two frontier nodes to estimate a RP, it does not generally have the same tangent as SE-GSM, where the tangent consists of a few specific ICs used as driving coordinates.

This difference in tangent definition and its influence on the outcome of a calculation is most pronounced in Reactions 10-a, 14-c, 15-a, and 16-b. Reaction 10-a is a representative example that describes addition of a hydrogen atom to oxygen of CO on Ni(111) surface to release H_2O and deposit C on the surface. SE-GSM's initial RP is formed under a more free reaction tangent compared to DE-GSM, because its reaction tangent consists of only one driving coordinate (addition of hydrogen and oxygen).

This freedom of movement in SE-GSM ultimately results in variations in energies and chemical structures of the TSs. In this example, SE-GSM results in a lower activation barrier and a more stable product (Fig. 4). This occurs because the CO molecule is stationary in DE-GSM, while it moves from its starting binding site to a neighboring fcc site in the SE-GSM case (Supporting Information Figure S9). Chemical structures of this example are quantitatively compared in Table 2. A similar situation happens in other cases (reactions 14-c, 15-a, 16-b) where the products form on different binding sites or in different relative positions on the surface.

In addition to different single elementary step transformations, we observed that reactions 4 and 5-b proceed in different number of elementary steps through the two GSM growth strategies. For example in reaction 4, CO and O combine on a Ru(0001) surface to release carbon dioxide. For this case, the DE-GSM's RP consists of two elementary steps, in which a CO-O complex is formed on the surface followed by its desorption. Conversely, the SE-GSM's RP proceeds through a single elementary step that combines CO_2 formation and desorption

(Fig. 5) through the asymmetric dissociation of Ru—O bonds (Supporting Information Figure S10 and TS structures of Fig. 5b).

When a system has many degrees of freedom, multiple pathways connecting the same two qualitative chemical structures can be present. SE- and DE-GSM provide two varying growth methods due to their tangent definitions, which enables exploring alternative paths for a given reaction. This will be especially the case if multiple SE-GSM trials are attempted, which is a subject of future research and will be reported subsequently.

Atomic layer deposition of TiN on Cu(111)

Titanium Nitride (TiN) has many desirable properties that make it a good candidate as a wear-resistant coating or copper diffusion barrier in microelectronics.[139] To build TiN layers of controlled thickness, ALD is an especially useful technique. In ALD, alternating cycles of two self-limiting and complementary reactions utilize gaseous precursors to form ultrathin, conformal, and uniform films with monolayer control over the thickness.[140] Experimental studies[141,142] have shown that tetrakis(dimethylamido)titanium (TDMAT) and ammonia (NH_3) are good precursors for ALD of TiN. By first reacting NH_3 onto the surface in the form of NH_x units and their derivatives (N, N_2), the subsequent ALD cycle using TDMAT precursors attaches Ti-containing species to these surface sites. On repeating these cycles, TiN layers can be formed in a controlled fashion.

Little mechanistic information is available for this ALD reaction, hindering our ability to extend the scope and availability of new precursors and conditions for reaction. While some mechanistic information for related processes are available,[143,144] these fail to capture any specific details of the TiN ALD mechanism. Given this lack of information, SE-GSM is ideally suited for investigating this process because it starts from
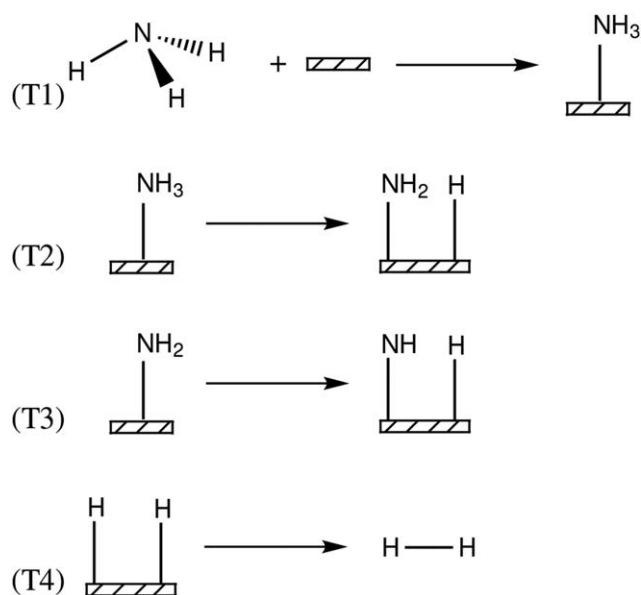

Figure 6. Proposed network of reactions for dehydrogenation of NH_3 on Cu(111).
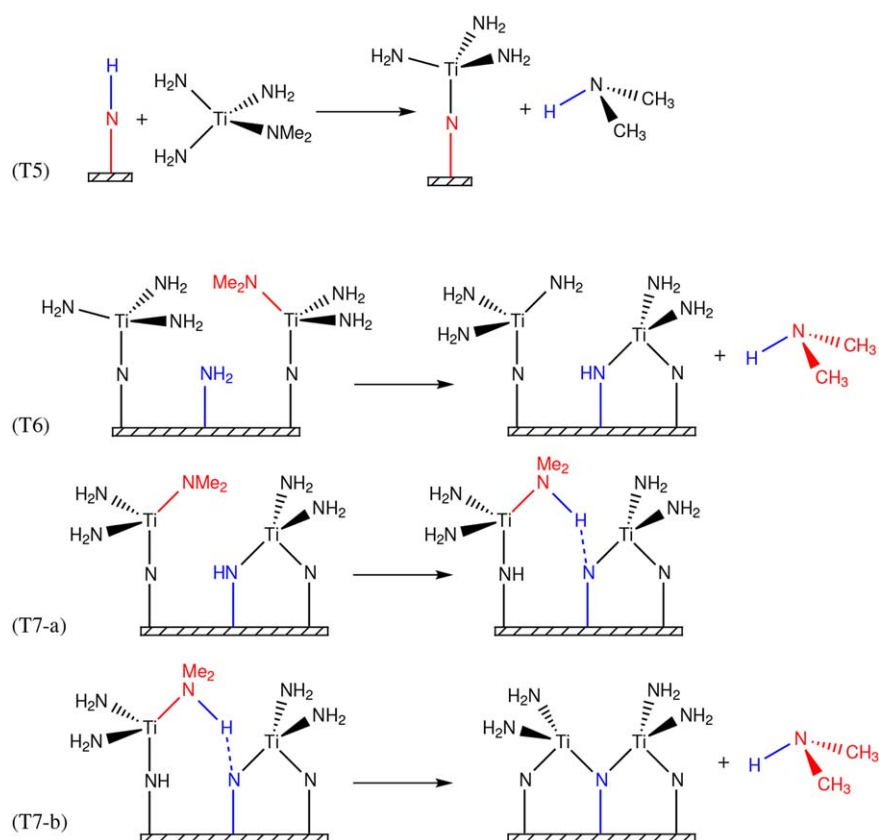
Figure 7. Proposed reactions during first TDMAT cycle. [Color figure can be viewed at wileyonlinelibrary.com]

a single initial state and locates the TS, RP, and the product in one computation. This capability enables systematic exploration of the reactive space, without requiring a guess transition structure close to the saddle point or even a complete set of reactive intermediates. Studying ALD of TiN will, therefore, serve to demonstrate the capabilities and advantages of SE-GSM for reactions that are not already well-known.

In particular, the initiation steps to form three atomic layers of TiN on Cu(111) will be studied. The reactive process

proposed here proceeds through three general steps: Step (1) Addition of ammonia to nucleate surface sites and release H_2 gas. Step (2) Deposition of titanium via a ligand-exchange with TDMAT extruding dimethylamine gas. Step (3) Addition of ammonia to the titanium-terminated surface. Repeating steps 2 and 3 provides access to additional layers of TiN. To reduce the computation complexity, $-N(CH_3)_2$ ligands are truncated to $-NH_2$ except when the ligand is involved directly in a reaction. A summary of activation energies, proposed reactions, and

Reactant-6   TS-6   Product-6

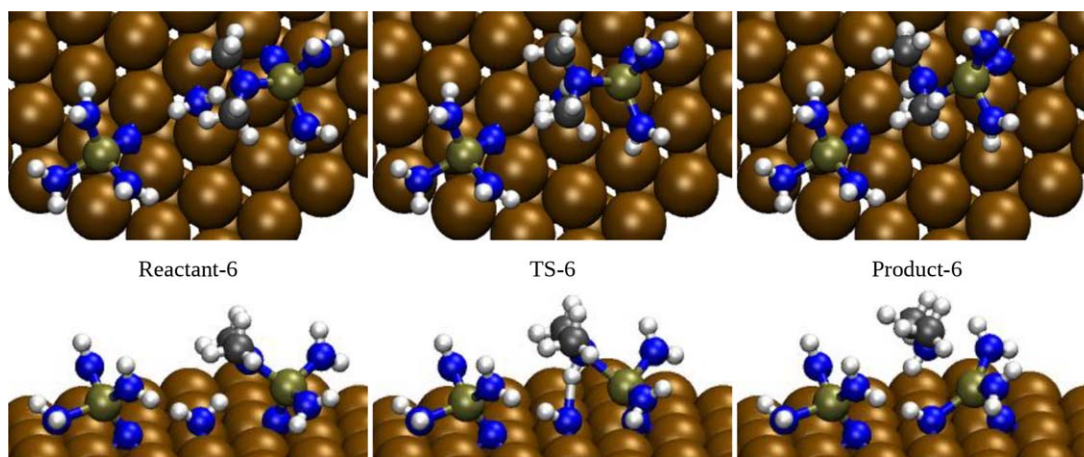**Figure 8.** Reactants, TS, and products of Reaction (T6). After adsorption of two TDMAT molecules on surface, they connect by a bridging N* that comes from an NH_2 species adsorbed on surface. In this reaction, one of the adsorbed tris(dimethylamido)titanium species reacts with NH_2^*. Atoms are N (blue), H (white), C (gray), Ti (tan green), and Cu (ochre). [Color figure can be viewed at wileyonlinelibrary.com]

Table 3. Activation energies and heat of reactions for the elementary steps of ALD of TiN on Cu(111).

ID	E_a (kcal/mol)	$\Delta E_{reaction}$ (kcal/mol)
T1	–	−10.6
T2	31.4	16.8
T3	30.5	27.6
T4	22.6	5.4
T5	7.9	−13.5
T6	19.3	4.4
T7-a	24.0	22.8
T7-b	9.7	8.9
T8	29.9	10.0
T9	29.1	20.2

chemical structures are shown in Table 3 and Figures 6 to 9 and Supporting Information Figures and S11 to S14. The asterisk (*) on chemical moieties means they are adsorbed on surface.

Nitrogen nucleation during first NH₃ cycle. During the first deposition cycle, molecular NH₃ is chemisorbed on the surface in a barrierless transformation that is exothermic by 10.6 kcal/mol (T1, Fig. 6). Three different orientations of adsorbed NH₃ are possible on surface which yield slightly different activation energies for the subsequent reactions. Reaction T1 is followed by progressive dehydrogenation of NH₃ to form NH_x^* species ($x = 2, 1, 0$) and subsequent release of H₂ gas from hydrogen adatoms present on the surface (Reactions T2-T4 of Fig. 6) as suggested by experimental studies.[141] During the first dehydrogenation step (T2, Fig. 6 and Supporting Information Figure S12a), NH_3^* moves from atop position to form NH_2^* in a higher-coordinated bridge site and H* in fcc through a barrier of 31.4 kcal/mol and is endothermic by 16.8 kcal/mol. A second hydrogen dissociation and migration from NH_2^* proceeds through a very similar process with a barrier of 30.5 kcal/mol and is also endothermic by 27.6 kcal/mol (T3, Fig. 6 and Supporting Information Figure S12b).

Although the barriers for fragmentation of surface bound ammonia are too high to proceed at room temperature, the experimental conditions can exceed 150°C, making these barriers surmountable. The barrier for reductive-coupling of two surface-bound hydrogen adatoms is 22.6 kcal/mol, which allows release of hydrogen gas and provides an entropic driving force for these reactions (T4, Fig. 6 and Supporting Information Figure S12c).

Ti layer formation. The second ALD cycle introduces TDMAT to the reaction. A previous report[142] on this process proposes that NH* moieties on surface likely serve as nucleation sites for TDMAT deposition, rather than open Cu surface sites. This step is, therefore, driven by the electron-rich dimethylamido ligands on TDMAT which serve as strong H-bond acceptors for NH* groups. This characteristic also means that its dimethylamido ligands make TDMAT preferable to other titanium precursors such as Ti(NH₂)₄. As a result, deposition of titanium on the surface (T5, Fig. 7) is initiated by the gradual formation of a strong H-bond between one of the dimethylamido ligands and an NH*. As the reaction approaches the TS, the hydrogen from NH* is formally transferred to dimethylamine, resulting in elongation of the titanium-amino bond by 0.20 Å. Additionally, the distance between the titanium center and the N*, 2.95 Å, is too long to be a covalent bond, highlighting the importance of a strong H-bond interaction to stabilize these types of species (Supporting Information Figure S11). The resulting Ti(N(CH₃)₂)₃(NH(CH₃)₂) intermediate is stabilized by interaction between one of the dimethylamido ligands on TDMAT and a surface amine, in this case N*. The final step of tethering titanium onto the surface, via ligation of N*, proceeds through a concerted ligand-exchange with a barrier of 7.9 kcal/mol, displacing one of the dimethylamido ligands via a dissociative transformation (Supporting Information Figure S13a). This mechanism is in agreement with the experimental observation of the build-up of dimethylamine gas during this process.[141,142]

Once the titanium is surface-bound through N*, it is plausible that further hydrogen-transfer/ligand-exchange reactions could lead to the formation of complex Ti-N bonding-networks. Such networks are suggested by the crystal structure of TiN, where titanium is coordinated to six nitrogens. Specifically, a dimethylamido ligand on titanium can undergo a hydrogen-transfer reaction with its neighboring unreacted NH_2^*
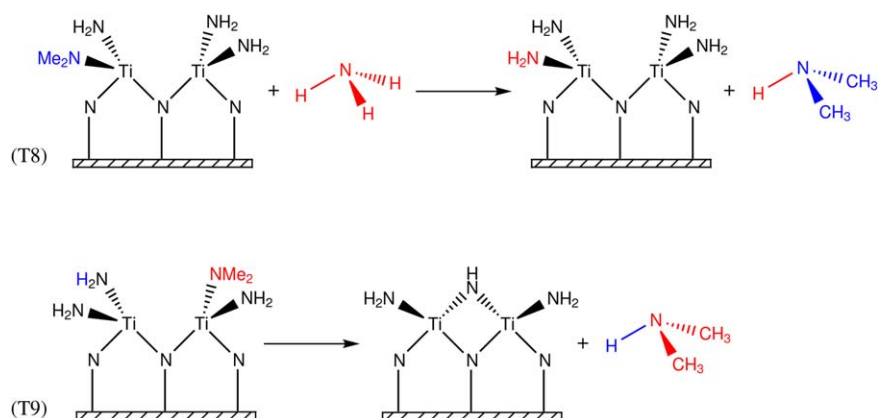
Figure 9. Second NH₃ cycle. [Color figure can be viewed at wileyonlinelibrary.com]

fragments (Reaction T6, Fig. 7) through concerted hydrogen-transfer/ligand-exchange. This transformation, which is similar to the initial TDMAT attachment step, adds another tethering site for titanium to bind to the surface. This second N-ligand-exchange with titanium has a barrier of 19.3 kcal/mol and is endothermic by 4.4 kcal/mol with a thermodynamic driving-force via release of the gaseous dimethylamine. Similar to Reaction T5, formation of N-H H-bonds in the reactant and TS structures facilitates proton transfer from NH_2^* to $N(CH_3)_2$ ligand in a dissociative concerted mechanism. After completion of proton transfer, a new bond between Ti and N* starts to form while breaking the Ti dimethylamine bond, resulting in a five coordinated titanium center before desorption of dimethylamine gas.

Although ligand-exchange pathways described so far have all been concerted, the formation of N*-bridged complex connecting two adjacent titanium species proceeds through a two-step process. The observation of a step-wise hydrogen transfer followed by ligand-exchange is likely a result of increasing steric demand of the incoming NH*. Nevertheless, the first step in this transformation is a hydrogen-transfer from NH* to the dimethylamido of titanium (Reaction T7-a, TS = 24.0 kcal/mol) resulting in a dimethylamine ligand on titanium (Reaction T7a, Supporting Information Figure S13b). The second step which is formation of Ti-N-Ti chain proceeds through a facile (Reaction T7-b, TS = 9.7 kcal/mol) associative ligand-exchange releasing the dimethylamine gas (Reaction T7b, Supporting Information Figure S13c).

Second NH_3 cycle. The alternating cycles of the ALD process require a third step of NH_3 exposure. Through a transamination reaction, SE-GSM shows that the topmost fragments of the deposited layers and the incoming NH_3 react through a step-wise process with an activation energy of 29.9 kcal/mol (Reaction T8, Fig. 9). Initially, hydrogen-transfer from NH_3^* to one of the dimethylamido ligands of Ti results in a dimethyl-amine ligand and formation of NH_2^*. This step is followed by addition of NH_2^* to one of the Ti centers and cleavage of the $Ti-NH(CH_3)_2$ bond to replace a dimethylamido ligand with an amido group (Supporting Information Figure S14a). Similar to Reaction T5, networks of H-bonds stabilize NH_3 over the surface during this reaction. Reaction T9 of Figure 9 is the final step in forming the third atomic layer, where a binding site for the incoming TDMAT of the fourth cycle is available. Hydrogen-transfer from the amido group to a dimethylamido ligand of a nearby Ti results in a bridged NH group and desorption of dimetylamine gas, with a barrier of 29.1 kcal/mol (Supporting Information Figure S14b).

These calculations suggest nucleation of the first Cu-N sites is rate-limiting. After this event, formation of H-bonds between ligands, moieties in the gas phase, and intramolecular H-bonds stabilize the various reactive intermediates and allow the deposition to proceed. Overall, the computed activation barriers are feasible given the high temperature reaction conditions, but desorption of gaseous products is a necessary step for most of these reactions to be favorable thermodynamically.

Conclusions

Surface reactions cover an important branch of chemistry that contains a wide variety of interesting processes. In this area, GSM is found to be a powerful method for the study of reactions due to its accuracy, reliability, fast convergence, and relative ease of use. The four components for success, strategies for quickly approaching the vicinity of the saddle point, estimation of the direction of negative curvature, optimizer, and coordinate system, were carefully considered, and together integrated into GSM for surfaces to make a method that is highly proficient at RP finding.

GSM's efficacy was confirmed by comparison with CI-NEB on an extensive set of reactions characteristic of modern surface chemistry studies. In these cases, GSM reduces the computational cost (in terms of gradient computations) by about 45% on average over CI-NEB.

In addition to high efficiency, GSM has the advantage of operating in single-ended way to enable explorative study of chemical reactions. The strength of the SE-GSM for the study of novel reactions was demonstrated in this article via the first study of ALD of TiN on Cu(111), which provided a wealth of details about the operating mechanism for deposition. In the future, the use of a combinatorial set of driving coordinates in surface SE-GSM to guide a reaction to many different outcomes will be possible through systematic graphical methods.[50,51]

APPENDIX

Hybrid coordinate system

The B matrix in primitive coordinates is formed using standard techniques[18]

$$B_{ij} = \frac{\partial q_i}{\partial x_j} \tag{6}$$

$$\Delta q = B \Delta X \tag{7}$$

where q are the primitive (hybrid) coordinates and X are Cartesians. The G matrix is formed and diagonalized as described below to produce a set of 3N NR (linearly independent) vector space, U.

$$G = BB^\top \tag{8}$$

$$G(U\ R) = (U\ R)\begin{pmatrix} \Lambda & 0 \\ 0 & 0 \end{pmatrix} \tag{9}$$

The B matrix in NR (hybrid) coordinates is formed based on

$$B^{NR} = U^\top B, U \in \mathbb{R}^{3N} \tag{10}$$

For the constraint optimization, the constraint vector, U_C, is formed by projecting the unit vector C corresponding to the constant primitive coordinates onto the full NR subspace

$$U_C = \sum_{k=1}^{3N} \langle C | U_k \rangle U_k \qquad (11)$$

The constraint vector, U_C, is normalized and the set V with $3N + 1$ vectors is formed by concatenating vectors U_k and the vector U_C

$$V = \{U_C, U_k; k = 1, \cdots, 3N\} \qquad (12)$$

Schmidt orthonormalization is carried out to form a new set (V^*) with $3N$-1 vectors U_k and the vector U_C

$$V_k^* = \alpha_k \left(V_k - \sum_{l=1}^{k-1} \langle V_k | V_l^* \rangle V_l^* \right) \qquad (13)$$

where α_k is a normalization constant, V_k are the vectors from the set V, and vectors V_l^* compose the new orthonormal basis, V^*.[12,86]

Hessian construction and update at each node

An initial diagonal Hessian in primitive coordinates is constructed from bonds, angles, and torsions and maintained to build a new NR coordinates Hessian after each update and reparameterization step. This procedure is enforced because NR coordinates change as reparameterization proceeds. The NR coordinates Hessian, H, at each node is created by applying change of basis to the Hessian in primitive coordinates (H^{prim})

$$H = U^\top H^{\text{prim}} U \qquad (14)$$

where U is the NR coordinates matrix. Both Hessians are updated using the BFGS[106–109] scheme

$$\Delta H_{\text{BFGS}} = \frac{\Delta g \Delta g^\top}{\Delta g^\top \Delta x} - \frac{H_{i-1} \Delta x \Delta x^\top H_{i-1}}{\Delta x^\top H_{i-1} \Delta x} \qquad (15)$$

where H_{i-1} is the Hessian of the previous step, and Δg and Δx are changes in current and previous gradient and coordinates, respectively. Note that Δg and Δx are in their respective NR coordinate or primitive coordinate basis for each corresponding Hessian matrix.

Hessian construction and update at TS node

After completion of CI, the exact TS search starts by constructing a Hessian with desired eigenvalue structure from TS node's existing Hessian. The curvature, C, along the RP at the TS node is approximated using the two neighboring nodes to estimate the TS eigenvector[111]

$$C = \frac{2E_{\text{TS}-1}}{a(a+b)} - \frac{2E_{\text{TS}}}{ab} + \frac{2E_{\text{TS}+1}}{b(a+b)} \qquad (16)$$

where $E_{\text{TS}-1}$ and $E_{\text{TS}+1}$ are the energies of the nodes prior to and following the TS node, E_{TS} is the energy of the TS node, a

is the distance between the TS and the previous node, and b is the distance to the following node.

This modification is applied by subtracting the curvature along the reaction tangent from C, and multiplying it by a symmetric matrix with proper size, $U_C U_C^\top$,

$$\Delta H = (C - U_C^\top H U_C) U_C U_C^\top \qquad (17)$$

The new Hessian is updated using the Bofill[112] method, which allows negative eigenvalues

$$\Delta H_{\text{Bofill}} = \phi \Delta H_{\text{MS}} + (1 - \phi) \Delta H_{\text{PSB}} \qquad (18)$$

$$\Delta H_{\text{MS}} = \frac{(\Delta g - H_{i-1} \Delta x)(\Delta g - H_{i-1} \Delta x)^\top}{(\Delta g - H_{i-1} \Delta x)^\top \Delta x} \qquad (19)$$

$$\Delta H_{\text{PSB}} = \frac{(\Delta g - H_{i-1} \Delta x) \Delta x^\top + \Delta x (\Delta g - H_{i-1} \Delta x)^\top}{\Delta x^\top \Delta x}$$
$$- \frac{\Delta x^\top (\Delta g - H_{i-1} \Delta x) \Delta x \Delta x^\top}{(\Delta x \Delta x^\top)^2} \qquad (20)$$

$$\phi = \frac{\left((\Delta g - H_{i-1} \Delta x)^\top \Delta x \right)^2}{|\Delta g - H_{i-1} \Delta x|^2 |\Delta x|^2} \qquad (21)$$

where H_{i-1}, Δg, and Δx are the same variables as described for eq. (15).

Acknowledgments

[1] S. M. George, *Chem. Rev.* **2010**, *110*, 111.
[2] N. Mizuno, M. Misono, *Chem. Rev.* **1998**, *98*, 199.
[3] W. J. Thomas, J. M. Thomas, *Principles and Practice of Heterogeneous Catalysis*; Wiley, **2014**. Available at: http://www.wiley.com/WileyCDA/WileyTitle/productCd-352729239X.html.
[4] A. M. Appel, J. E. Bercaw, A. B. Bocarsly, H. Dobbek, D. L. DuBois, M. Dupuis, J. G. Ferry, E. Fujita, R. Hille, P. J. A. Kenis, C. A. Kerfeld, R. H. Morris, C. H. F. Peden, A. R. Portis, S. W. Ragsdale, T. B. Rauchfuss, J. N. H. Reek, L. C. Seefeldt, R. K. Thauer, G. L. Waldrop, *Chem. Rev.* **2013**, *113*, 6621.
[5] D. Poppinger, *Chem. Phys. Lett.* **1975**, *35*, 550.
[6] C. J. Cerjan, *J. Chem. Phys.* **1981**, *75*, 2800.
[7] J. Simons, P. Joergensen, H. Taylor, J. Ozment, *J. Phys. Chem.* **1983**, *87*, 2745.
[8] J. Baker, *J. Comput. Chem.* **1986**, *7*, 385.
[9] P. Pulay, G. Fogarasi, *J. Chem. Phys.* **1992**, *96*, 2856.
[10] D. J. Wales, *J. Chem. Soc. Faraday Trans.* **1992**, *88*, 653.
[11] J. Baker, *J. Comput. Chem.* **1993**, *14*, 1085.

[12] J. Baker, A. Kessi, B. Delley, *J. Chem. Phys.* **1996**, *105*,

[13] J. Baker, F. Chan, *J. Comput. Chem.* **1996**, *17*, 888.

[14] A. Banerjee, N. Adams, J. Simons, R. Shepard, *J. Phys. Chem.* **1985**, *89*, 52.

[15] G. Henkelman, H. Jonsson, *J. Chem. Phys.* **1999**, *111*, 7010.

[16] S. R. Billeter, A. J. Turner, W. Thiel, *Phys. Chem. Chem. Phys.* **2000**, *2*, 2177.

[17] B. Paizs, J. Baker, S. Suhai, P. Pulay, *J. Chem. Phys.* **2000**, *113*, 6566.

[18] V. Bakken, T. Helgaker, *J. Chem. Phys.* **2002**, *117*, 9160.

[19] A. Laio, M. Parrinello, *Proc. Natl. Acad. Sci. USA* **2002**, *99*, 12562.

[20] E. M. Muller, A. de Meijere, H. Grubmuller, *J. Chem. Phys.* **2002**, *116*, 897.

[21] M. Iannuzzi, A. Laio, M. Parrinello, *Phys. Rev. Lett.* **2003**, *90*, 238302.

[22] B. Peters, W. Liang, A. T. Bell, A. Chakraborty, *J. Chem. Phys.* **2003**, *118*, 9533.

[23] H. B. Schlegel, *J. Comput. Chem.* **2003**, *24*, 1514.

[24] A. Heyden, A. T. Bell, F. J. Keil, *J. Chem. Phys.* **2005**, *123*, 224101.

[25] B. Ensing, M. De Vivo, Z. Liu, P. Moore, M. L. Klein, *Acc. Chem. Res.* **2006**, *39*, 73.

[26] X. Li, M. J. Frisch, *J. Chem. Theory Comput.* **2006**, *2*, 835.

[27] H. B. Schlegel, *Adv. Chem. Phys.* **2007**, *3*, 249.

[28] J. M. Del Campo, A. M. Köster, *J. Chem. Phys.* **2008**, *129*, 024107.

[29] E. Cancès, F. Legoll, M. C. Marinica, K. Minoukadeh, F. Willaime, *J. Chem. Phys.* **2009**, *130*, 114711.

[30] S. Maeda, K. Ohno, K. Morokuma, *J. Chem. Theory Comput.* **2009**, *5*, 2734.

[31] S. K. Burger, P. W. Ayers, *J. Chem. Phys.* **2010**, *132*, 234110.

[32] W. Liang, H. Wang, J. Hung, X. Li, M. J. Frisch, *J. Chem. Theory Comput.* **2010**, *6*, 2034.

[33] S. Maeda, K. Morokuma, *J. Chem. Theory Comput.* **2011**, *7*, 2335.

[34] H. B. Schlegel, *Wiley Interdiscip. Rev. Comput. Mol. Sci.* **2011**, *1*, 790.

[35] M. Chen, M. A. Cuendet, M. E. Tuckerman, *J. Chem. Phys.* **2012**, *137*, 024102.

[36] S. Maeda, E. Abe, M. Hatanaka, T. Taketsugu, K. Morokuma, *J. Chem. Theory Comput.* **2012**, *8*, 5058.

[37] J. W. May, J. D. Lehner, M. J. Frisch, X. Li, *J. Chem. Theory Comput.* **2012**, *8*, 5175.

[38] A. Samanta, E. Weinan, *J. Chem. Phys.* **2012**, *136*, 124104.

[39] J. Baker, P. M. W. Gill, *J. Comput. Chem.* **1988**, *9*, 465.

[40] R. Abagyan, M. Totrov, D. Kuznetsov, *J. Comput. Chem.* **1994**, *15*, 488.

[41] M. Totrov, R. Abagyan, *J. Comput. Chem.* **1994**, *15*, 1105.

[42] A. F. Voter, *Phys. Rev. Lett.* **1997**, *78*, 3908.

[43] P. G. Bolhuis, D. Chandler, C. Dellago, P. L. Geissler, *Annu. Rev. Phys. Chem.* **2002**, *53*, 291.

[44] R. A. Olsen, G. J. Kroes, G. Henkelman, A. Arnaldsson, H. Jonsson, *J. Chem. Phys.* **2004**, *121*, 9776.

[45] C. Herrmann, M. Reiher, *Surf. Sci.* **2006**, *600*, 1891.

[46] J. Kästner, P. Sherwood, *J. Chem. Phys.* **2008**, *128*, 014106.

[47] M. P. Haag, A. C. Vaucher, M. Bosson, S. Redon, M. Reiher, *ChemPhysChem* **2014**, *15*, 3301.

[48] Y. Zeng, P. Xiao, G. Henkelman, *J. Chem. Phys.* **2014**, *140*, 044115.

[49] P. Xiao, J. Duncan, L. Zhang, G. Henkelman, *J. Chem. Phys.* **2015**, *143*, 244104.

[50] P. M. Zimmerman, *Mol. Simul.* **2015**, 43, 4.

[51] P. M. Zimmerman, *J. Comput. Chem.* **2013**, *34*, 1385.

[52] M. Bergeler, C. Herrmann, M. Reiher, *J. Comput. Chem.* **2015**, *36*, 1429.

[53] A. B. Birkholz, H. B. Schlegel, *J. Comput. Chem.* **2015**, *36*, 1157.

[54] P. M. Zimmerman, *J. Comput. Chem.* **2015**, *36*, 601.

[55] C. Peng, H. Bernhard Schlegel, *Isr. J. Chem.* **1993**, *33*, 449.

[56] G. Mills, H. Jónsson, *Physical Review Letters* **1994**, *72*, 1124.

[57] C. Peng, P. Y. Ayala, H. B. Schlegel, M. J. Frisch, *J. Comput. Chem.* **1996**, *17*, 49.

[58] P. Y. Ayala, H. B. Schlegel, *J. Chem. Phys.* **1997**, *107*, 375.

[59] G. Henkelman, H. Jonsson, *J. Chem. Phys.* **2000**, *113*, 9978.

[60] G. Henkelman, B. P. Uberuaga, H. Jonsson, *J. Chem. Phys.* **2000**, *113*, 9901.

[61] W. E. Ren, E. Vanden-Eijnden, *Phys. Rev. B* **2002**, *66*, 4.

[62] H. Jónsson, G. Mills, K. W. Jacobsen, Nudged Elastic Band Method for Finding Minimum Energy Paths of Transitions in Classical and Quantum Dynamics in Condensed Phase Simulations, Ed. B. J. Berne, G. Ciccotti and D. F. Coker, 385 (World Scientific, **1998**).

[63] J. W. Chu, B. L. Trout, B. R. Brooks, *J. Chem. Phys.* **2003**, *119*, 12708.

[64] S. A. Trygubenko, D. J. Wales, *J. Chem. Phys.* **2004**, *120*, 2082.

[65] B. Peters, A. Heyden, A. T. Bell, A. Chakraborty, *J. Chem. Phys.* **2004**, *120*, 7877.

[66] W. E. E, W. Ren, E. Vanden-Eijnden, *J. Phys. Chem. B* **2005**, *109*, 6688.

[67] W. Quapp, *J. Chem. Phys.* **2005**, *122*, 174106.

[68] S. K. Burger, W. Yang, *J. Chem. Phys.* **2006**, *124*, 054109.

[69] R. Ren, G. Orkoulas, *J. Chem. Phys.* **2007**, *126*, 211102.

[70] S. K. Burger, W. Yang, *J. Chem. Phys.* **2007**, *127*, 164107.

[71] W. E. Ren, E. Vanden-Eijnden, *J. Chem. Phys.* **2007**, *126*, 164103.

[72] A. Goodrow, A. T. Bell, M. Head-Gordon, *J. Chem. Phys.* **2008**, *129*, 174109.

[73] D. Sheppard, R. Terrell, G. Henkelman, *J. Chem. Phys.* **2008**, *128*, 134106.

[74] R. Granot, R. Baer, *J. Chem. Phys.* **2008**, *128*, 184111.

[75] J. Klimeš, D. R. Bowler, A. Michaelides, *J. Phys.: Condens. Matter* **2010**, *22*, 074203.

[76] Y. Liu, S. K. Burger, P. W. Ayers, *J. Math. Chem.* **2011**, *49*, 1915.

[77] S. A. Ghasemi, S. Goedecker, *J. Chem. Phys.* **2011**, *135*, 014108.

[78] A. Behn, P. M. Zimmerman, A. T. Bell, M. Head-Gordon, *J. Chem. Theory Comput.* **2011**, *7*, 4019.

[79] A. Behn, P. M. Zimmerman, A. T. Bell, M. Head-Gordon, *J. Chem. Phys.* **2011**, *135*, 224108.

[80] P. Tao, M. Hodošček, J. D. Larkin, Y. Shao, B. R. Brooks, *J. Chem. Theory Comput.* **2012**, *8*, 5035.

[81] H. Chaffey-Millar, A. Nikodem, A. V. Matveev, S. Krueger, N. Roesch, *J. Chem. Theory Comput.* **2012**, *8*, 777.

[82] S. Mallikarjun Sharada, P. M. Zimmerman, A. T. Bell, M. Head-Gordon, *J. Chem. Theory Comput.* **2012**, *8*, 5166.

[83] J. Jung, S. Re, Y. Sugita, S. Ten-no, *J. Chem. Phys.* **2013**, *138*, 044106.

[84] W. Ren, E. Vanden-Eijnden, *J. Chem. Phys.* **2013**, *138*, 134105.

[85] P. Plessow, *J. Chem. Theory Comput.* **2013**, *9*, 1305.

[86] P. M. Zimmerman, *J. Chem. Phys.* **2013**, *138*, 184102.

[87] D. G. Truhlar, B. C. Garrett, *Acc. Chem. Res.* **1980**, *13*, 440.

[88] D. G. Truhlar, B. C. Garrett, *Annu. Rev. Phys. Chem.* **1984**, *35*, 159.

[89] P. L. Fast, D. G. Truhlar, *J. Chem. Phys.* **1998**, *109*, 3721.

[90] G. Henkelman, G. Jóhannesson, H. Jónsson, In *Theoretical Methods in Condensed Phase Chemistry*; Dordrecht: Kluwer Academic Publishers, **2002**; pp. 269–302. Available at: http://link.springer.com/10.1007/0-306-46949-9_10 Accessed October 15, 2016.

[91] E. Vanden-Eijnden, M. Venturoli, *J. Chem. Phys.* **2009**, *130*, 194103.

[92] A. Goodrow, A. T. Bell, M. Head-Gordon, *J. Chem. Phys.* **2009**, *130*, 244108.

[93] D. Sheppard, P. Xiao, W. Chemelewski, D. D. Johnson, G. Henkelman, *J. Chem. Phys.* **2012**, *136*, 074103.

[94] A. B. Birkholz, H. B. Schlegel, *Theor. Chem. Acc.* **2012**, *131*, 1170.

[95] I. V. Khavrutskii, J. B. Smith, A. Wallqvist, *J. Chem. Phys.* **2013**, *139*, 165104.

[96] N. A. Zarkevich, D. D. Johnson, *J. Chem. Phys.* **2015**, *142*, 024106.

[97] X. J. Zhang, Z. P. Liu, *J. Chem. Theory Comput.* **2015**, *11*, 4885.

[98] A. B. Birkholz, H. B. Schlegel, *J. Chem. Phys.* **2015**, *143*, 244101.

[99] P. Zimmerman, *J. Chem. Theory Comput.* **2013**, *9*, 3043.

[100] A. Pedersen, S. F. Hafstein, H. Jónsson, *SIAM J. Sci. Comput.* **2011**, *33*, 633.

[101] I. H. Williams, G. M. Maggiora, *J. Mol. Struct.: THEOCHEM* **1982**, *89*, 365.

[102] C. Lanczos, *J. Res. Natl. Bur. Stand.* **1950**, *45*, 255.

[103] E. R. Davidson, *J. Comput. Phys.* **1975**, *17*, 87.

[104] S. M. Sharada, A. T. Bell, M. Head-Gordon, *J. Chem. Phys.* **2014**, *140*, 164115.

[105] A. B. Birkholz, H. B. Schlegel, *Theor. Chem. Acc.* **2016**, *135*, 84.

[106] R. Fletcher, *Comput. J.* **1970**, *13*, 317.

[107] C. G. Broyden, *IMA J. Appl. Math.* **1970**, *6*, 222.

[108] D. Goldfarb, *Math. Comput.* **1970**, *24*, 23.

[109] D. F. Shanno, *Math. Comput.* **1970**, *24*, 647.

[110] H. B. Schlegel, *Int. J. Quantum Chem.* **1992**, *44*, 243.

[111] E. V. Anoshkina, A. G. Belyaev, H. Seidel, In *Proceedings of the Vision, Modeling, and Visualization Conference 2002 (VMV 2002)*, Erlangen, Germany, November 20–22, **2002**; pp. 211–216.

[112] J. M. Bofill, *J. Comput. Chem.* **1994**, *15*, 1.

[113] J. D. Head, *J. Comput. Chem.* **1990**, *11*, 67.

[114] H. Nakano, T. Nakajima, S. Obara, *Chem. Phys. Lett.* **1991**, *177*, 458.

[115] G. Kresse, J. Hafner, *Phys. Rev. B* **1993**, *48*, 13115.

[116] G. Kresse, J. Furthmüller, *Comput. Mater. Sci.* **1996**, *6*, 15.

[117] G. Kresse, J. Furthmüller, *Phys. Rev. B* **1996**, *54*, 11169.

[118] G. Kresse, D. Joubert, *Phys. Rev. B* **1999**, *59*, 1758.

[119] S. Bahn, K. Jacobsen, *Comput. Sci. Eng.* **2002**, *4*, 56.

[120] S. Piccinin, M. Stamatakis, *ACS Catal.* **2014**, *4*, 2143.

[121] Y. Matsumoto, T. Amano, T. N. Kato, M. Hoshino, *Science* **2015**, *347*, 974.

[122] J. Lu, S. Behtash, A. Heyden, *J. Phys. Chem. C* **2012**, *116*, 14328.

[123] C. Wang, Y. J. Yang, J. Jiang, D. S. Tsai, H. M. Hsieh, *J. Phys. Chem. C* **2009**, *113*, 17411.

[124] Q. Zhang, B. Han, X. Tang, K. Heier, J. X. Li, J. Hoffman, M. Lin, S. L. Britton, A. Derecskei-Kovacs, H. Cheng, *J. Phys. Chem. C* **2012**, *116*, 16522.

[125] G. C. Wang, J. Nakamura, *J. Phys. Chem. Lett.* **2010**, *1*, 3053.

[126] G. Wang, L. Jiang, C. Pan, Z. W. Huang, Xie, L. Sun, B. Zhong, *J. Phys. Chem. B* **2003**, *107*, 557.

[127] A. A. Gokhale, J. A. Dumesic, M. Mavrikakis, *J. Am. Chem. Soc.* **2008**, *130*, 1402.

[128] C. Callaghan, I. Fishtik, R. Datta, M. Carpenter, M. Chmielewski, A. Lugo, *Surf. Sci.* **2003**, *541*, 21.

[129] S. F. Peng, J. J. Ho, *J. Phys. Chem. C* **2010**, *114*, 19489.

[130] H. Chen, D. G. Musaev, M. C. Lin, *J. Phys. Chem. C* **2007**, *111*, 17333.

[131] G. M. Mullen, L. Zhang, E. J. Evans, T. Yan, G. Henkelman, C. B. Mullins, *J. Am. Chem. Soc.* **2014**, *136*, 6489.

[132] D. Mei, L. Xu, G. Henkelman, *J. Phys. Chem. C* **2009**, *113*, 4522.

[133] X. Hu, J. Yin, R. J. Meyer, M. Trenary, *J. Phys. Chem. C* **2015**, *119*, 14506.

[134] F. A. Soria, E. M. Patrito, P. Paredes-Olivera, *J. Phys. Chem. C* **2013**, *117*, 18021.

[135] G. Henkelman, H. Jónsson, *Phys. Rev. Lett.* **2001**, *86*, 664.

[136] S. Y. Kim, I. H. Lee, S. Jun, *Phys. Rev. B* **2007**, *76*, 245408.

[137] C. Mattevi, H. Kim, M. Chhowalla, *J. Mater. Chem.* **2011**, *21*, 3324.

[138] S. Q. Wang, *MRS Bull.* **1994**, *19*, 30.

[139] J. Musschoot, Q. Xie, D. Deduytsche, S. Van den Berghe, R. Van Meirhaeghe, C. Detavernier, *Microelectron. Eng.* **2009**, *86*, 72.

[140] F. Zaera, *J. Mater. Chem.* **2008**, *18*, 3521.

[141] D. Longrie, D. Deduytsche, J. Haemers, P. F. Smet, K. Driesen, C. Detavernier, *ACS Appl. Mater. Interfaces* **2014**, *6*, 7316.

[142] J. Elam, M. Schuisky, J. Ferguson, S. George, *Thin Solid Films* **2003**, *436*, 145.

[143] S. D. Elliott, *Semicond. Sci. Technol.* **2012**, *27*, 074008.

[144] J. B. Cross, H. Schlegel, *Chem. Phys. Lett.* **2001**, *340*, 343.